Check for updates

Cadmium Substitution Effect on Microstructure and Magnetic Properties of Mg-Cu-Zn Ferrites

Morteza Beyranvand, Ahmad Zahedi and Ahmad Gholizadeh*

School of Physics, Damghan University, Damghan, Iran

The microstructure, optical, and magnetic properties of $Cd_xMg_{0.3-x}Cu_{0.2}Zn_{0.5}Fe_2O_4$ ferrites prepared by the citrate auto-combustion method were investigated. The samples were analyzed by X-ray diffraction, scanning electron microscopy, UV-Vis spectroscopy, https://soh.iums.ac.ir/uploads/uv-vis_-_2.pptx X-ray energy-dispersive spectroscopy, Fourier-transform infrared spectroscopy, and vibrating sample magnetometer. Rietveld refinement of XRD patterns shows a single-phase cubic structure (space group $Fd\overline{3}m$) for the samples with x up to 0.20, while the impurity phase of CdO is observed in the samples with $x = 0.25, 0.30$. As the substitution content increases, the presence of non-magnetic Cd^{2+} ions in the octahedral site and the migration of Fe^{3+} ions from the octahedral site to the tetrahedral site decreases the saturation magnetization of the samples. Comparison of the bandgap energy of the samples shows an increasing trend with Cd substitution for x up to 0.20 and then decreases, which can be interpreted in terms of changes in the electronic structure of the samples. Improvement in dielectric properties of the samples with increase of Cd^{2+} content for x up to 0.20 may be attributed to easier transfer and electron exchange between Fe^{3+} and M^{2+} ions.

Keywords: Mg-Cu-Zn spinel ferrite, microstructure, saturation magnetization, citrate-nitrate method, dielectric properties, elastic properties

INTRODUCTION

Magnetism and magnetic materials have attracted enormous interest since the discovery of the phenomenon of giant magnetic resistance (GMR) in multilayer structures. In these structures, the ferromagnetic layer is coupled to a magnetic metallic layer with 1–3 nm thick (Mollamahaleh et al., 2011; T. Rahal et al., 2017). With the advent of magnetic nanotechnology, small magnetic materials are made with improved magnetic properties (Navaei Diva et al., 2017). The main applications of magnetic nanomaterials are using in the construction of data storage mediums, small electric motors, and magnetic nanofluids (Noori and Gholizadeh, 2019; Esmaili and Gholizadeh, 2020). Nowadays, the most common use of magnetic nanomaterial is related to magnetic nano-powders, because by decreasing the dimensions of the powder particles, the quality of the magnetic devices also improves (Chen and He, 2001; Son et al., 2002). The industrialization of countries has led to the increasing extraction of hazardous heavy metals such as lead, Mercury, and arsenic. As a result, the production of metal superparamagnetic particles from iron oxide nanoparticles to adsorb these heavy metals using their magnetic properties has been considered (Chen et al., 2003; Noori and Gholizadeh, 2019). The optimal properties of magnetic nanostructures are high mechanical strength, high permeability, low core loss (up to about 25% of normal values), high saturation magnetization (M_s), excellent temperature stability, etc. (Gopal Reddy et al., 1999; El-Kemary et al., 2013). Among different spinel

ferrites reported in literature, the spinel ferrite nanoparticles have been the subject of nanotechnology researchers due to their unique properties. Spinel ferrites have the general formula $[M^{2+}] [Fe^{3+}] O_4$, in which M is the divalent metal cations such as Zn, Ni, Mn, Cu, etc. (Manikandan et al., 2014). Structural, magnetic, electrical, and catalytic properties of spinel ferrites depend on ionic radii and their distribution on the octahedral (B) and tetrahedral (A) sites of the spinel structure (Manikandan et al., 2013a).

In a spinel structure, the B site is larger than the A site. Bivalent ions are larger than trivalent ions, so it is reasonable that, divalent ions are in the B sites and trivalent ions are in the A sites. But there is an exception in zinc ferrite ($ZnFe_2O_4$) that larger divalent ions tend to occupy the A sites because their electronic arrangements are more suitable for A-site binding to lattice oxygen ions (Gill and Puri, 1985; El-Sayed, 2002; Manikandan et al., 2013b). The zinc ferrite is a semiconductor material with a high electrical resistance that does not conduct DC (Manikandan et al., 2013b). $ZnFe_2O_4$ is used for many applications, such as catalytic and photocatalytic activity (Manikandan et al., 2014), magnetic resonance imaging, and ferrofluids (Abareshi et al., 2010; Manikandan et al., 2013c). In $Zn_{1-x}Cu_xFe_2O_4$ nanoparticles, a part of the Cu^{2+} and Zn^{2+} ions occupy the B sites and some of the smaller Fe^{3+} ions may be distributed in the A sites instead of the larger Cu^{2+} and Zn^{2+} ions (Banerjee et al., 2007; Ajmal and Maqsood, 2008).

Previous studies on $Mg_xMn_{0.3-x}Cu_{0.2}Zn_{0.5}Fe_3O_4$ nanoparticles prepared by the citrate auto-combustion method show Mg^{+2} ions can be substituted in the A- and B-sites, but preferably tend to occupy the A site, while Fe^{+3} ions occupy both the sites (Shamgani and Gholizadeh, 2019). Manganese also had a strong tendency to occupy both the sites. In Ni-Cu-Zn ferrite nanoparticles, the nickel ion only tends to occupy the B site, while the Cu^{+2} occupy both the A and B sites. (Gholizadeh and Jafari, 2017). substituting the Cu^{+2} ions for Ni^{+2} at the B site, resulted in a decrease of the M_s. In addition, the results showed that the conclusion of the random distribution of the cations in both the A and B sites, the amount of magnetization in these two sites was subject to change. Studies showed that Mg^{+2} ions can be substituted on the A and B sites in $Mg_{0.3-x}Ba_xCu_{0.2}Zn_{0.5}Fe_3O_4$, ferrite, but preferably tend to occupy the A sites and, Fe^{+3} ions are on both the sites (Gholizadeh and Beyranvand, 2020). Because the ionic radius of Ba^{+2} is larger than the other divalent cations in the A and B sites, it is expected that Ba^{+2} will sit more in the B site. Also, studies on $Mn_{0.3-x}Cd_xCu_{0.2}Zn_{0.5}Fe_3O_4$ nanoparticles showed that Mn^{+2} and Fe^{+3} ions can occupy both the A and B sites (Beyranvand and Gholizadeh, 2020). Since the ionic radius of Cd^{+2} is greater than the other divalent cations in the A and B sites, it is expected that cadmium ions will occupy the B site. In this paper, the aim is to discuss the structural, optical and magnetic properties of $Mg_{0.30-x}Cd_xCu_{0.2}Zn_{0.5}Fe_2O_4$ spinel ferrites with x = 0.00, 0.05, 0.10, 0.15, 0.20, 0.25, 0.30.

EXPERIMENTAL

Preparation of $Cd_xMg_{0.3-x}Cu_{0.2}Zn_{0.5}Fe_2O_4$ Ferrites

First, the appropriate mole of $Mg(NO_3)_2 \cdot 4H_2O$, $Cd(NO_3)_2 \cdot 4H_2O$, $Cu(NO_3)_2 \cdot 3H_2O$, $Zn(NO_3)_2 \cdot 4H_2O$, $Fe(NO_3)_3 \cdot 9H_2O$ according to

Table 1, with citric acid (1:1 mole ratio), was completely dissolved with a minimum of water and its pH value noted as 2 (Gholizadeh, 2017b; Gholizadeh and Malekzadeh, 2017; Gholizadeh, 2019). Then, the resulted solution was put in an oven for 24 h at 80°C and kept until complete drying. After that, the dried materials were powdered and finally calcined at 500°C for 3 h.

Characterization of the Samples

X-ray diffraction patterns (XRD) of the powders were recorded using Bruker's Advanced-8D at room temperature (RT) in the range of 2θ = 20–80°. XRD device was equipped with a Cu-Kα (λ = 1.5404 Å) radiation source and a nickel filter (35 mA, 30 kV). Fourier-transform infrared (FTIR) spectra of the samples were measured with Perkin-Elmer device at RT. The crystal structure and lattice parameters were determined by a Rietveld method using the Fullprof program. Halder-Wagner (H-W) method was employed for calculating the crystallite size (D) and microstrain (ε) of the samples (Gholizadeh et al., 2016):

$$\left(\frac{\beta^*_{hkl}}{d^*_{hkl}}\right)^2 = \left(\frac{\varepsilon}{2}\right)^2 + \left(\frac{\beta^*_{hkl}}{d^{*2}_{hkl}}\right)\left(\frac{1}{D}\right) \qquad (1)$$

where, $\frac{\beta_{hkl}\cos\theta}{\lambda} = \beta^*_{hkl}$ and $\frac{2\sin\theta}{\lambda} = d^*_{hkl}$. The surface images of the samples were recorded by the field-emission scanning electron microscope (FE-SEM, MlRA3 model), and the values of average particle sizes were calculated from the FESEM images by digimizer image analysis software. Also, the atomic and weight percentage of the constituent elements of the compound was calculated by the X-Ray energy dispersive (EDX) spectroscope equipped inside the FE-SEM microscope. To study the optical properties of the samples, the absorption spectra of these nanoparticles were obtained by UV-Vis spectroscopy (UNICO model 4,802) in the UV-Vis region. The energy gap of the samples was obtained using Tauc's method according to Ref. (Gholizadeh and Tajabor, 2010). The magnetic hysteresis loop of the samples was measured at RT using a vibrating sample magnetometer (VSM, 7,400 Lake Shore) and in a variable magnetic field up to 2T. The powders were compressed into pallets with diameter 14 mm and sintered at 500 °C for 1 h. Then pellets were coated by Ag in order to investigate the electrical behaviour. The dielectric measurements were performed in the frequency range (100 Hz-10 MHz) using a precision LCR meter (GW Instek 8110G).

RESULTS AND DISCUSSION

Structural Features

XRD pattern of $Cd_xMg_{0.3-x}Cu_{0.2}Zn_{0.5}Fe_2O_4$ nanoparticles are shown in **Figure 1**. The Miller indices (hkl) of the spinel phase are labeled on the diffraction peaks in **Figure 1**, which corresponds to the (220), (311), (222), (400), (422), (511), (440) planes. Structural analysis of samples x = 0.00, 0.05, 0.10, 0.15, 0.20, using X'pert package indicates the formation of a pure cubic spinel structure with $Fd\overline{3}m$ space group, which is in agreement with JCPDS standard cards numbered 47-2,399 (Beyranvand and Gholizadeh, 2020; Gholizadeh and Beyranvand, 2020). However,

TABLE 1 | Moles of the metal nitrates to prepare the $Mg_{0.3-x}Cd_xCu_{0.2}Zn_{0.5}Fe_2O_4$.

Sample	$Mg(NO_3)_2 \cdot 4H_2O$	$Cd(NO_3)_2 \cdot 4H_2O$	$Cu(NO_3)_2 \cdot 3H_2O$	$Zn(NO_3)_2 \cdot 4H_2O$	$Fe(NO_3)_3 \cdot 9H_2O$
$x = 0.00$	0.00262	—	0.00175	0.00437	0.0262
$x = 0.05$	0.00214	0.000429	0.00171	0.00429	0.0257
$x = 0.10$	0.00168	0.000843	0.00168	0.00421	0.0252
$x = 0.15$	0.00124	0.00124	0.00165	0.00413	0.0248
$x = 0.20$	0.00081	0.00162	0.00162	0.00406	0.0243
$x = 0.25$	0.000399	0.00199	0.00159	0.00399	0.0239
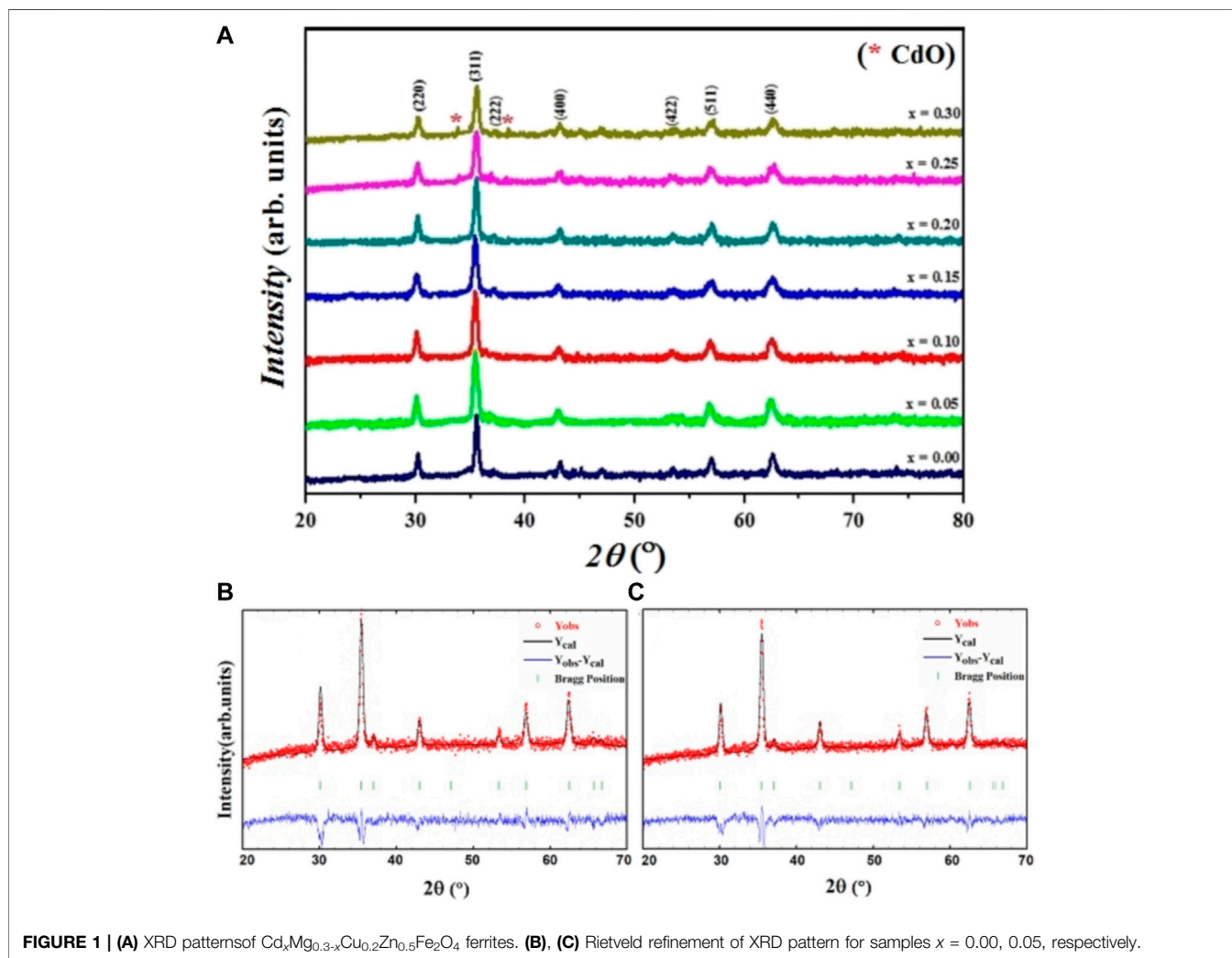
FIGURE 1 | (A) XRD patternsof $Cd_xMg_{0.3-x}Cu_{0.2}Zn_{0.5}Fe_2O_4$ ferrites. **(B)**, **(C)** Rietveld refinement of XRD pattern for samples $x = 0.00$, 0.05, respectively.

this analysis for samples with $x = 0.25$, 0.30 indicates the presence of CdO impurity phase in addition to spinel phase diffraction peaks as shown in **Figure 1**. For more detailed structural studies, Rietveld refinement of X-ray diffraction patterns using Fullprof software for the samples was performed to calculate the lattice parameter of the unit cell.

The lattice parameter values (*a*) of all the samples are given in **Table 2**, and the change in the *a* with the Cd content is drawn in **Figure 2**. The *a* shows a decreasing trend by increasing the amount of cadmium from $x = 0.00$ to $x = 0.15$, and then the

substitution goes through an increasing trend. The ionic radii of the atoms participating in the A-site (CN: 4) for Mg^{2+}, Cd^{2+}, Zn^{2+}, Cu^{2+}, Zn^{2+}, Fe^{2+}, Fe^{3+}, O^{2-} are: 0.49, 0.84, 0.62, 0.60, 0.63, 0.49, 1.38 Å, respectively, and in the B site (CN: 6) are: 0.72, 0.95, 0.73, 0.74, 0.77, 0.64, 1.40 Å, respectively (William, 1944; Birajdar et al., 2002). It is observed that the lattice parameter decreases with cadmium content obeying Vegard's law for *x* up to 0.15 (Bachhav et al., 2011). However, as reported by the structural analysis, there is the traces of CdO impurity phase in addition to spinel phase diffraction peaks for $x = 0.25$, 0.30. This result shows

TABLE 2 | The a, D_{H-W}, and ε, dislocation density (δ), theoretical and experimental density, porosity percentage, mean particle size (D_{FESEM}), and as well as R-factors values related to the quality of Rietveld refinement.

Sample	a (Å)	D_{H-W} (nm)	$\varepsilon \times 10^3$ (unitless)	ρ_{XRD} (g/cm^3)	ρ_{exp} (g/cm^3)	P (%)	D_{FESEM} (nm)	δ (×1014 m^2)	R-factors (%)			
									R_p	R_{wp}	R_{exp}	χ^2
x = 0.00	8.413 (1)	26.78 (2)	3.89 (6)	5.292	5.101	4.7 (8)	36.0 (0)	13.9	2.60	3.61	2.08	3.01
x = 0.05	8.406 (5)	25.08 (7)	5.03 (8)	5.393	5.282	3.4 (4)	32.9 (7)	15.9	2.37	3.24	2.16	2.25
x = 0.10	8.402 (2)	23.75 (1)	1.84 (5)	5.496	5.408	3.0 (5)	31.7 (4)	17.7	2.52	3.42	2.14	2.56
x = 0.15	8.400 (8)	22.41 (0)	6.45 (2)	5.597	5.564	2.0 (9)	29.7 (8)	19.9	2.63	3.58	2.12	2.86
x = 0.20	8.401 (5)	23.02 (3)	6.38 (8)	5.696	5.465	5.5 (6)	----	18.9	2.46	3.44	2.23	2.39
x = 0.25	8.402 (6)	25.34 (5)	4.63 (1)	5.798	5.656	3.9 (7)	----	15.6	2.95	4.24	2.23	3.63
x = 0.30	8.406 (9)	26.40 (1)	10.69 (6)	5.888	5.750	3.7 (9)	----	14.3	6.07	9.15	3.02	6.61
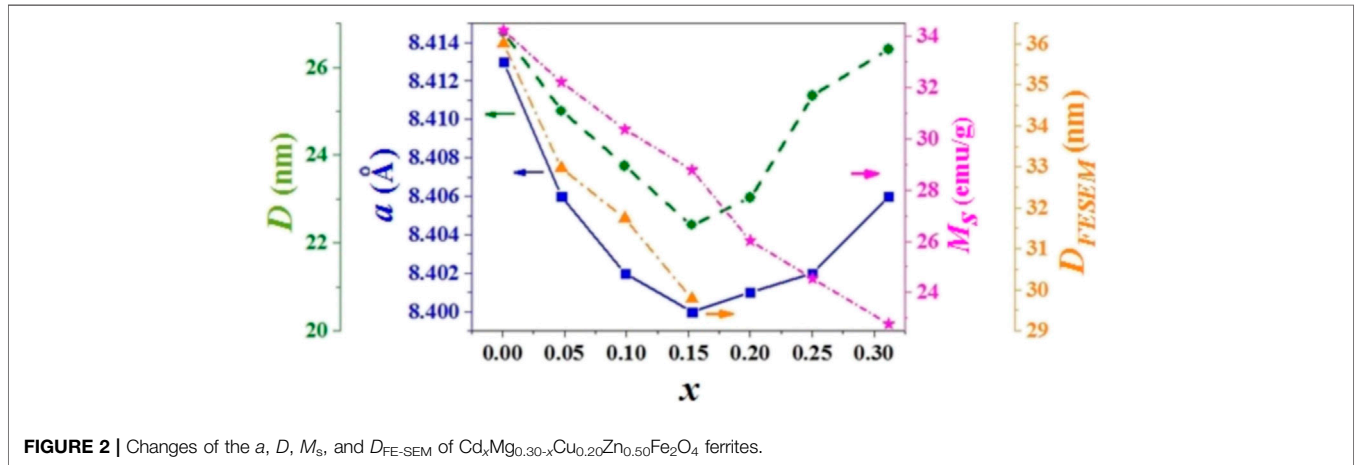
FIGURE 2 | Changes of the a, D, M_s, and D_{FE-SEM} of Cd$_x$Mg$_{0.30-x}$Cu$_{0.20}$Zn$_{0.50}$Fe$_2$O$_4$ ferrites.

that the solid solubility limit in our samples is for $x = 0.15$. Also, decrease in the lattice parameter a results in the decrease of the bond lengths with Cd content. It can be concluded that there is increase of ionic-covalent character of the spinel with Cd content (Yue et al., 2001; Bachhav et al., 2011).

The linear fitting curves of $(\frac{\beta_{hkl}^*}{d_{hkl}^*})^2$ versus $(\frac{\beta_{hkl}^*}{d_{hkl}^{*2}})$ in the H-W method are plotted for all samples in **Figure 3** (Gholizadeh and Jafari, 2017; Gholizadeh and Beyranvand, 2020). In the H-W method, the crystallite size values (D_{H-W}) and micro-strain (ε) were obtained using the slope inverse and the y-intercept of the linearly fitted data, respectively as given in **Table 2**. These results demonstrated that the lattice parameter shows dependence on size of particle, decreasing for smaller particles, increasing strain-surface effects (Bachhav et al., 2011).

The theoretical density (ρ_{XRD}) of Cd$_x$Mg$_{0.30-x}$Cu$_{0.20}$Zn$_{0.50}$Fe$_2$O$_4$ ferrites was obtained from the following equation (Gholizadeh, 2018):

$$\rho_{XRD} = \frac{8M}{N_A a^3} \quad (2)$$

In the above relation, M, and a are the molar mass, and the lattice parameter of the samples, respectively. An increase in the theoretical density with the Cd substitution shows that the increasing trend of the molar mass overcomes the non-uniform change of the a. Also, the experimental density (ρ_{exp}) of the studied ferrites was obtained by the following equation (Gholizadeh and Jafari, 2017):

$$A \times d = V \rightarrow \rho = \frac{m}{V} \quad (3)$$

In the above relation, A is the surface of the pellet, d is the thickness of the pellet, m is the weight of the pellet, V is also the pellet's volume. Using the theoretical and experimental densities of all samples, the values of porosity percentage (P) were calculated with the following relation (William, 1944):

$$P = \frac{\rho_{XRD} - \rho_{exp}}{\rho_{XRD}} \times 100 \quad (4)$$

The dislocation density (δ) contains information on the improvement of the crystal structure and was calculated according to $\delta = \frac{1}{D^2}$ (ZeidAbo Zeida et al., 2019). The values of dislocation density, theoretical density, experimental density, and porosity are given in **Table 2**. As can be seen from **Table 2**, there is approximately equal and low porosity in the studied ferrites. Also, one can notice the dependence of density on the Cd content. The density increases with increasing Cd content, indicating improved densification by incorporating Cd into the ferrite samples (Yue et al., 2001). Further, X-ray density of all the ferrite samples is higher than the corresponding bulk density, due to the existence of the voids and pores. The decrease in the dislocation density (δ) values and, consequently, the lattice strain, is caused by an increase in the Cd content (ZeidAbo Zeida et al., 2019). There is a decrease in the size of crystallites and an increase in the dislocation density of the samples. In this case, the resulting
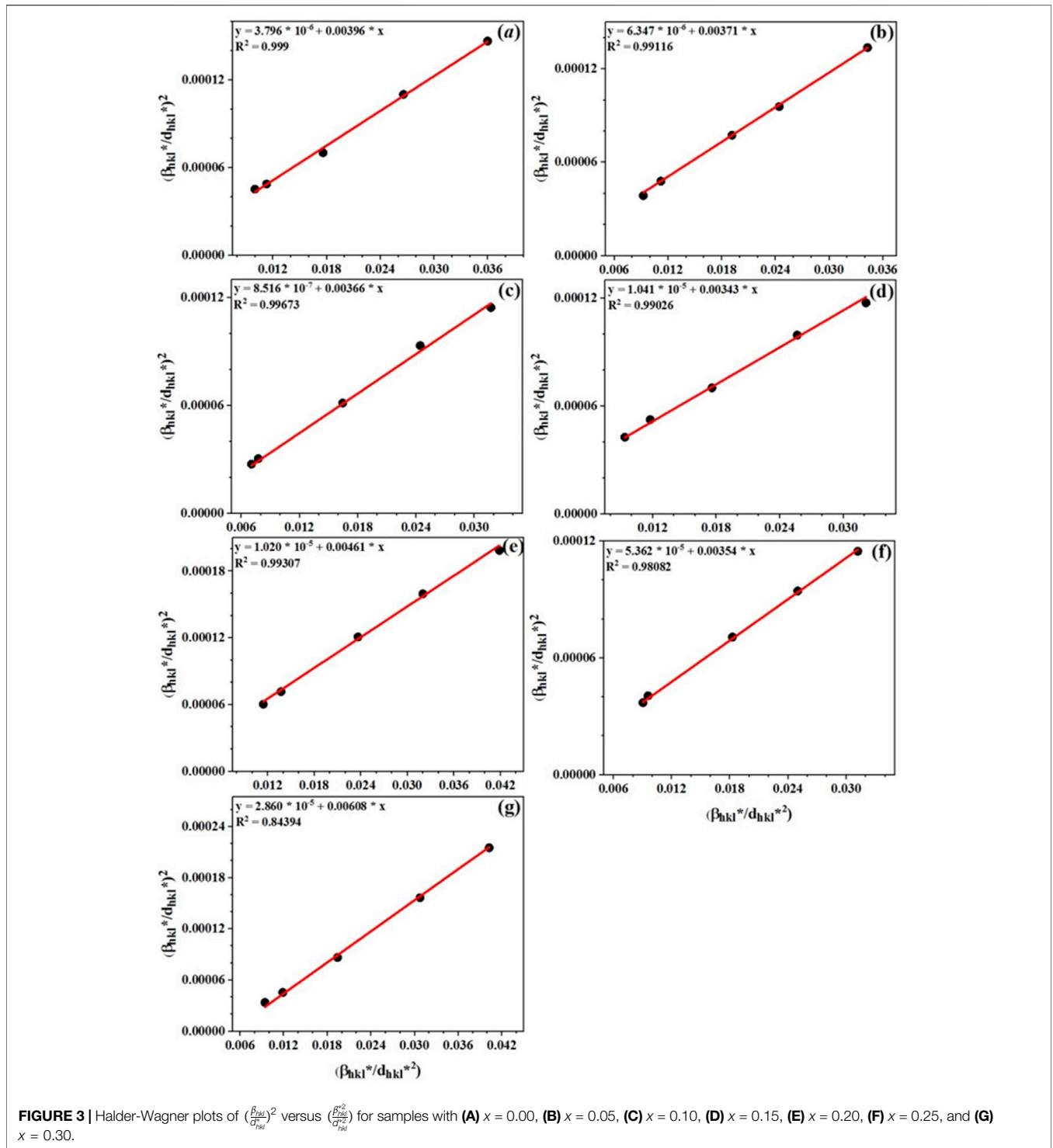
FIGURE 3 | Halder-Wagner plots of $\left(\frac{\beta_{hkl}^*}{d_{hkl}^*}\right)^2$ versus $\left(\frac{\beta_{hkl}^{*2}}{d_{hkl}^{*2}}\right)$ for samples with **(A)** $x = 0.00$, **(B)** $x = 0.05$, **(C)** $x = 0.10$, **(D)** $x = 0.15$, **(E)** $x = 0.20$, **(F)** $x = 0.25$, and **(G)** $x = 0.30$.

defects and dislocations result in distortion and deformation of the crystal lattice with the formation of disordered regions in the structure (ZeidAbo Zeida et al., 2019).

FESEM Images and EDX Analysis

The FE-SEM images of the samples with $x = 0.00$, 0.05, 0.10, 0.15 are shown in **Figure 4**. As can be seen, the surface morphology of

the samples consists of ordered grains composed of smaller nanoparticles with an unequal size that are distributed throughout the samples with small porosity. A particle size distribution diagram of the samples was drawn and the mean particle size (D_{FESEM}) was obtained using fitting the particle size distribution histogram with the lognormal distribution function (Mahmoudi and Gholizadeh, 2018).
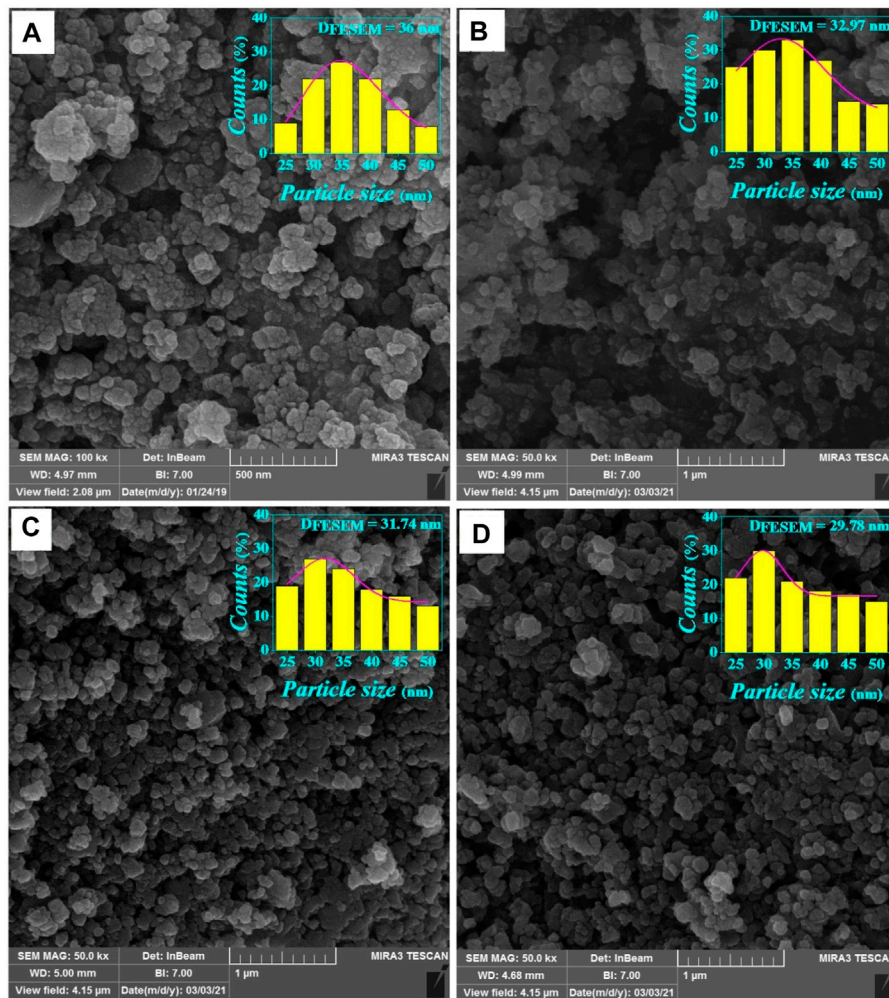
FIGURE 4 | The FE-SEM images and log-normal distribution diagram of $Cd_xMg_{0.30-x}Cu_{0.20}Zn_{0.50}Fe_2O_4$ for **(A)** $x = 0.00$, **(B)** $x = 0.05$, **(C)** $x = 0.10$, and **(D)** $x = 0.15$.

$$P(d) = \frac{1}{d\sigma_d\sqrt{2\pi}} \exp\left(-\frac{1}{2\sigma_d^2}\ln\left(\frac{d}{D_{FESEM}}\right)\right) \qquad (5)$$
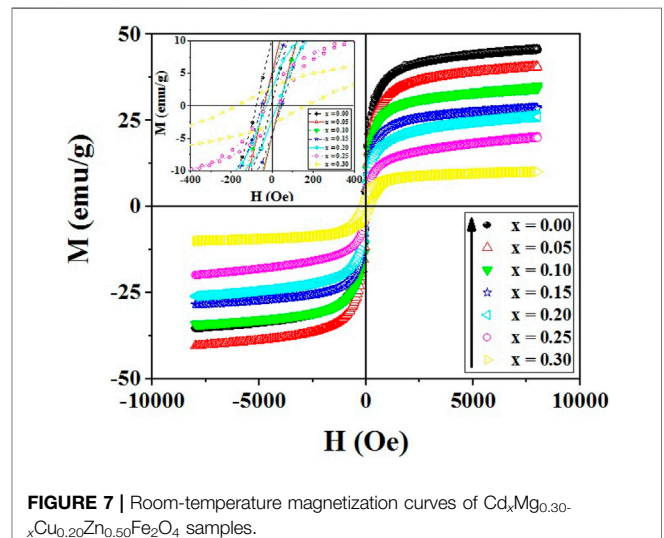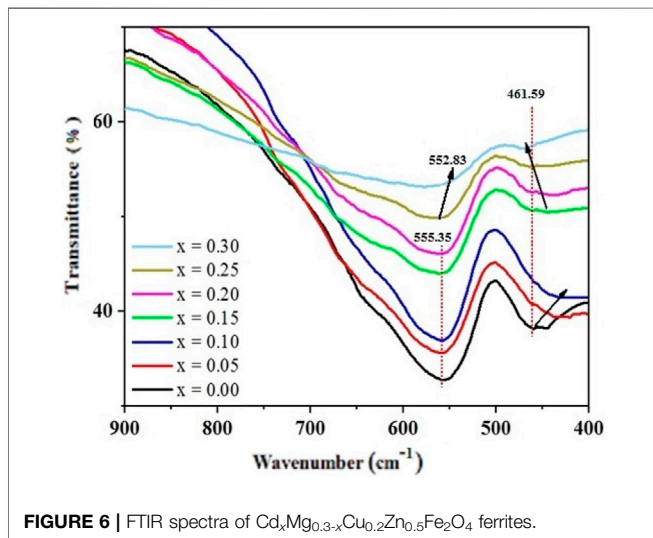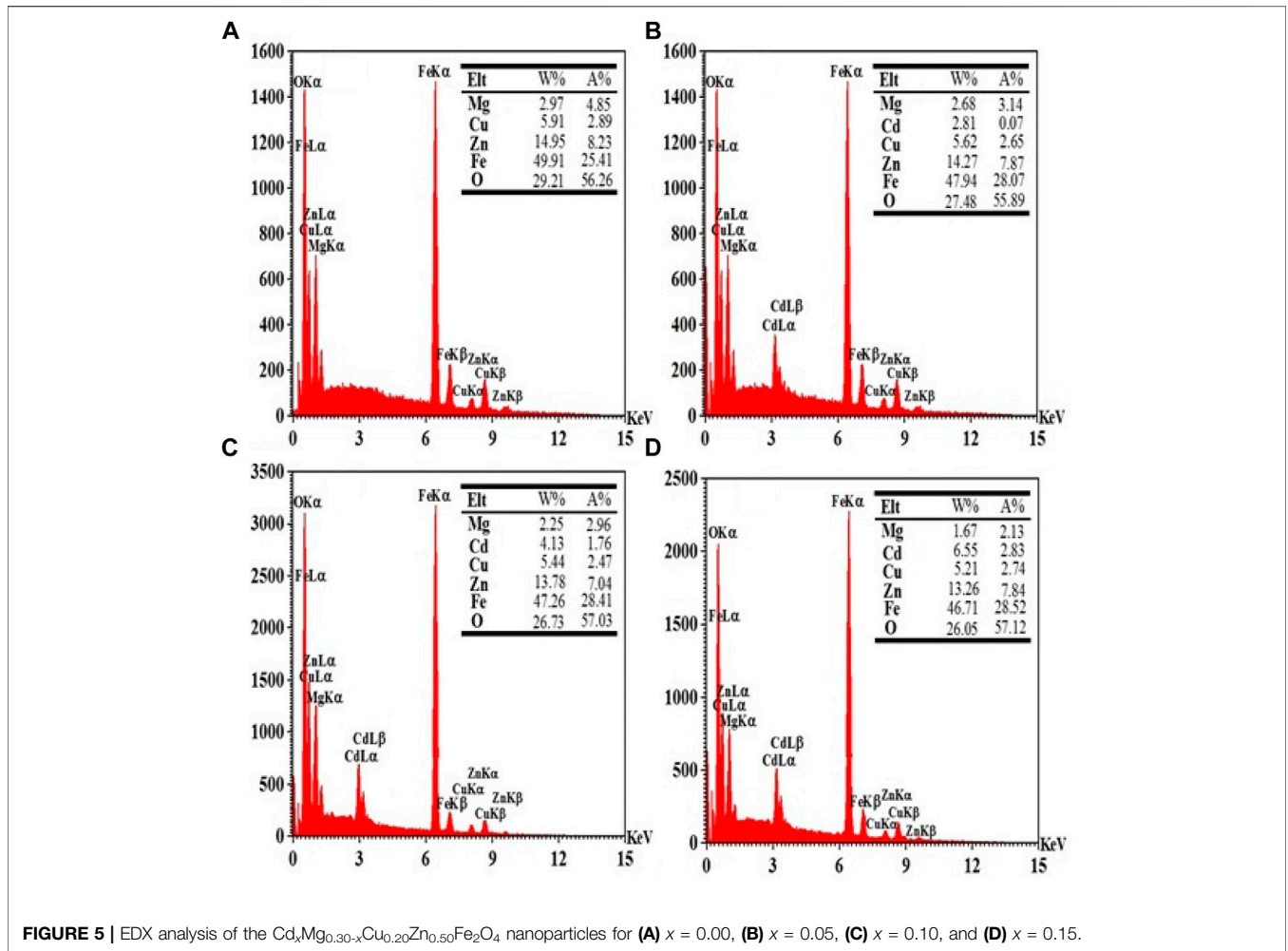
The D_{FESEM} values calculated are given in **Table 2** and are plotted in **Figure 2**. The particle size obtained by this method is slightly larger than the D_{H-W} obtained by the Halder-Wagner method. This is because the grains consist of crystallite size. As shown in **Figure 2**, the variation of the D_{FE-SEM} is compatible with the values of the a, and D_{H-W}.

The X-ray Energy-dispersive spectroscopy (EDX) attached to the FESEM microscope was used for elemental analysis of the samples. **Figure 5** shows the elemental analysis spectra obtained from the EDX analysis for $Cd_xMg_{0.30-x}Cu_{0.20}Zn_{0.50}Fe_2O_4$ nanoparticles. In the desired spectrum, energy lines related to Mg, Cd, Cu, Zn, Fe, O can be seen. The values of atomic percentage and weight percentage calculated from the spectrum for the constituent elements of the FESEM samples are recorded as a table in the inset of **Figure 5**. The data in these tables show a good agreement with the formula composition of each sample.

FTIR Analysis

The FTIR spectra of all samples are shown in **Figure 6** in the wavelength range of 400–900 cm^{-1}. Two strongly absorption bands are observed around 450 and 560 cm^{-1}, which are familiar to those that observed in the spinel ferrites and are mainly related to the iron-oxygen vibrations. The frequency band υ_t at around 560 cm^{-1} related to the oxygen-iron vibration at the A site, the frequency band υ_o around 450 cm^{-1} refers to the oxygen-iron vibration at the B site, so that the appearance of these two vibration modes confirms the formation of the spinel structure of the samples (Gholizadeh and Jafari, 2017). However, the position and width of the bands are affected by factors such as grain size, sintering conditions, and preparation method (Gholizadeh and Jafari, 2017).

As shown in **Figure 6**, the value of υ_t at the A site for the samples with $x = 0.00, 0.05, 0.10, 0.15, 0.20$ is almost constant, but υ_o at the B site for these samples shows a decreasing trend. However, the value of υ_t in the samples with $x = 0.25, 0.30$ shows a decreasing trend, and υ_o for these samples shows an

FIGURE 5 | EDX analysis of the $Cd_xMg_{0.30-x}Cu_{0.20}Zn_{0.50}Fe_2O_4$ nanoparticles for **(A)** $x = 0.00$, **(B)** $x = 0.05$, **(C)** $x = 0.10$, and **(D)** $x = 0.15$.

FIGURE 6 | FTIR spectra of $Cd_xMg_{0.3-x}Cu_{0.2}Zn_{0.5}Fe_2O_4$ ferrites.

FIGURE 7 | Room-temperature magnetization curves of $Cd_xMg_{0.30-x}Cu_{0.20}Zn_{0.50}Fe_2O_4$ samples.

increasing trend. The difference in the band's position can be interpreted in terms of the mass and radius of the participating atoms at the two sites. Here, the change in

the Fe^{3+}-O^{2-} bond length at the A and B sites explains the changes observed in the a. Since the ionic radius of Cd^{2+} is greater than other divalent cations participated at the A and B
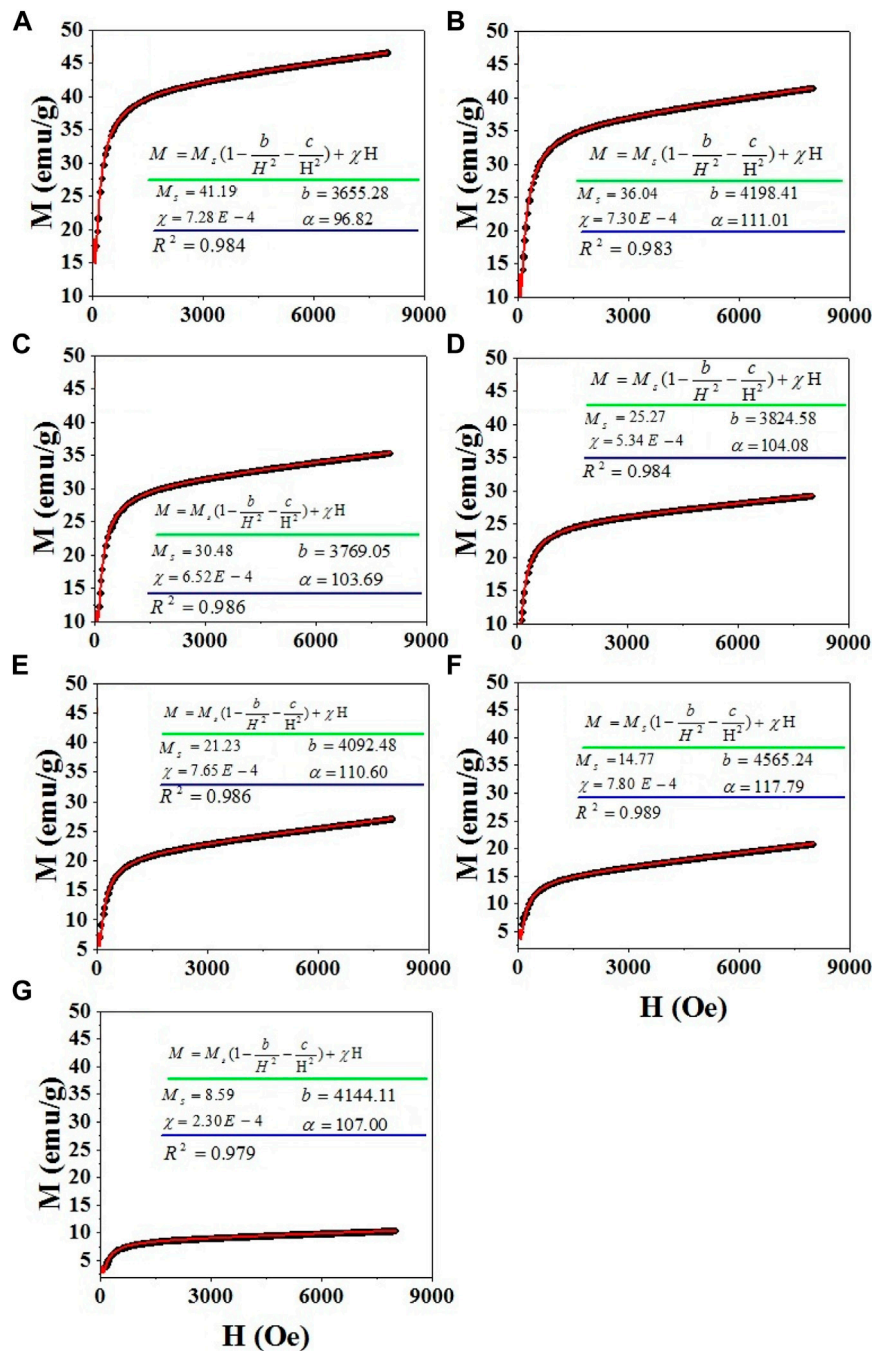
FIGURE 8 | LAS fitting of magnetization curves of $Cd_xMg_{0.30-x}Cu_{0.20}Zn_{0.50}Fe_2O_4$ nanoparticles for samples **(A)** $x = 0.00$, **(B)** $x = 0.05$, **(C)** $x = 0.10$, **(D)** $x = 0.15$, **(E)** $x = 0.20$, **(F)** $x = 0.25$, **(G)** $x = 0.30$.

sites, it can mainly occupy the B site, which explains the variation of the υ_2.

Magnetic Measurement

Figure 7 shows the magnetization curves of $Cd_xMg_{0.30-x}Cu_{0.20}Zn_{0.50}Fe_2O_4$ ferries versus applied magnetic field. The magnetic hysteresis confirms the prepared ferrite material is

magnetically ordered. The magnetic parameters of the studied ferrites can be obtained from these curves.

The According to law of approach to saturation (LAS), the magnetization of ferromagnetic nanoparticles at high magnetic fields follows the following formula (Gholizadeh and Jafari, 2017; Beyranvand and Gholizadeh, 2020; Gholizadeh and Beyranvand, 2020).

$$M(H) = M_s \left[1 - \left(\frac{b}{H^2} \right) - \left(\frac{c}{H^3} \right) \right] + \chi H \qquad (6)$$

where, M_s is the contribution of ferromagnetic saturation magnetization. The LAS fitting of the magnetization curves with this formula is shown in **Figure 8** for all the samples.

In general, the total M_s of the ferrites depends on the distribution of magnetic cations in the A and B sites, sintering temperature, grain size, chemical composition, density, etc. (Gholizadeh and Jafari, 2017; Gholizadeh, 2018; Shamgani and Gholizadeh, 2019; Beyranvand and Gholizadeh, 2020; Gholizadeh and Beyranvand, 2020). Magnetization of ferrites is strongly dependent on the exchange interactions between cations present at A and B sites. These exchange interactions are A–B, B–B and A–A interactions, either positive or negative. The parallel arrangement of cations is represented by positive and negative sign denotes anti-parallel arrangement of cations. These interactions depend on magnitude, sign, the extent and form of overlap of the 3d electron wave functions of the neighboring ions (Hakim et al., 2015; Vara Prasad, 2015; THORAT et al., 2018). The strength of the interaction is proportional to the distance between ions and the cations present in the ferrite system. Therefore, when the system is altered with larger/smaller cations it may influence the magnetization. Magnetization of ferrites also can be explained on Neel's theory of ferrimagnetism (two sub lattice model) (Hakim et al., 2015; Vara Prasad, 2015; THORAT et al., 2018). According to the Néel theory, the A-B negative exchange interaction dominates over the A-A and B-B positive exchange interactions. The magnetic moments in each sublattice are oriented in parallel and relative to each are antiparallel. According to Neil's theory, the M_s of the spinel ferrites can be expressed by (Gholizadeh and Jafari, 2017; Beyranvand and Gholizadeh, 2020; Gholizadeh and Beyranvand, 2020):

$$M_s = |M_B - M_A| \qquad (7)$$

where, M_A and M_B are the M_s of ions at the A- and B-sites, respectively. Two factor are determining the decrease of M_s with Cd content. First factor for a gradual decrease in the magnetization of the samples with the increasing the Cd^{2+} content is originated from the presence of non-magnetic Cd^{2+} ions at the B site which induces a pressure on the Fe^{3+} (5 μ_B) ions at the B site and their transfer to the A site. This reduces the magnetization of the samples in accordance with the Néel relation. Second factor in decrease of M_s with Cd content is the decrease of grain size. Since, magnetization caused by domain wall movement requires less energy than that requires by domain rotation, it is easy for the domain wall movement to magnetize or demagnetize the samples with larger grain size (Hakim et al., 2015). Samples with larger grain are expected to have high M_s. However, a high decrease in the M_s of the samples with $x = 0.25, 0.30$ can also be attributed to the CdO impurity phase. The CdO is the II-VI group semiconductor that shows the paramagnetism nature at RT. The coexistence of the CdO phase and spinel ferrite can potentially explain the decrease of M_s (Beyranvand and Gholizadeh, 2020).

Optical Properties

Investigation of optical properties of $Mg_{0.30-x}Cd_xCu_{0.2}Zn_{0.5}Fe_2O_4$ nanoparticles is possible by using the absorption spectrum of the samples in the visible-ultraviolet region. The direct energy gap of all the studied samples was obtained by extrapolating the linear part of the diagram of $(\alpha h\upsilon)^2$ versus $(h\upsilon)$ as shown in **Figure 9**. The error in bandgap value, measured from Tauc plot method is ~0.02 eV. The energy gap of the samples with increasing the Cd substitution up to $x = 0.20$ shows an increasing trend and then decreases with the substitution. The obtained values of the bandgap are in agreement with the values reported in other articles for ferrites (Ajmal and Maqsood, 2008; Banerjee et al., 2007). The energy gap of the samples may shift due to structural changes in the crystal lattice parameters listed in **Table 2** (Andrade et al., 2017). It can be interpreted in terms of the changes in the electronic structure of the samples which is originated from the changes in the $Fe^{3+}-O^{2-}-Fe^{3+}$ bond angle and the $Fe^{3+}-O^{2-}$ bond length. Also, **Figure 9** depicts that the energy band gap increases as the crystallite size decreases with the increase of Cdsubstitution for x up to 0.20 (see **Table 2**). Such behavior may be explained on the bases of Brass's effective mass model (Lin et al., 2005; Jauhar et al., 2011; Agrawal et al., 2016), where the measured band gap E_g^* can be expressed as a function of particle size as:

$$E_g^* = E_g^{bulk} + \frac{h^2}{8er^2} \left(\frac{1}{m_e} + \frac{1}{m_h} \right) - \frac{1.8\,e^2}{4\pi\varepsilon_o\,\varepsilon\,r} \qquad (8)$$

where E_g^{bulk} is the bulk energy gap, r is the particle size, m_e is the effective mass of electrons, m_h is the effective mass of holes, ε is the relative permittivity, ε_0 is the permittivity of free space, h is Planck constant and e is electron charge. According to this model, the energy band gap increases as the particle size decrease.

Dielectric Properties

The measured values of capacitance (C) and dielectric loss tangent (tan δ) of the pellets were used for obtaining the real (ε_r') and imaginary (ε_r'') dielectric constant by the following relations (Beyranvand and Gholizadeh, 2020; Gholizadeh and Beyranvand, 2020);

$$\varepsilon_r' = \frac{Ct}{\varepsilon_0 A} \qquad (9)$$

$$\varepsilon_r'' = \varepsilon_r' \tan \delta \qquad (10)$$

where t, and A are the thickness, and the surface area of the pellets. The ε_o is the permittivity of free space.

Changes in the real and imaginary component of the dielectric constant are shown in **Figure 10A,B** as a function of frequency for $Mg_{0.30-x}Cd_xCu_{0.2}Zn_{0.5}Fe_2O_4$ ($x = 0.00, 0.10, 0.20, 0.30$) ferrites. The ε' has larger values at low frequencies and then, the values of the dielectric constants decrease uniformly and become very low in the high frequency region which can be mainly interpreted with a Maxwell's theory of the interfacial polarization (Beyranvand and Gholizadeh, 2020). Based on the proposed mechanism for this type of polarization, the dielectric structure of the ferrites is generally divided into two layers; Layers
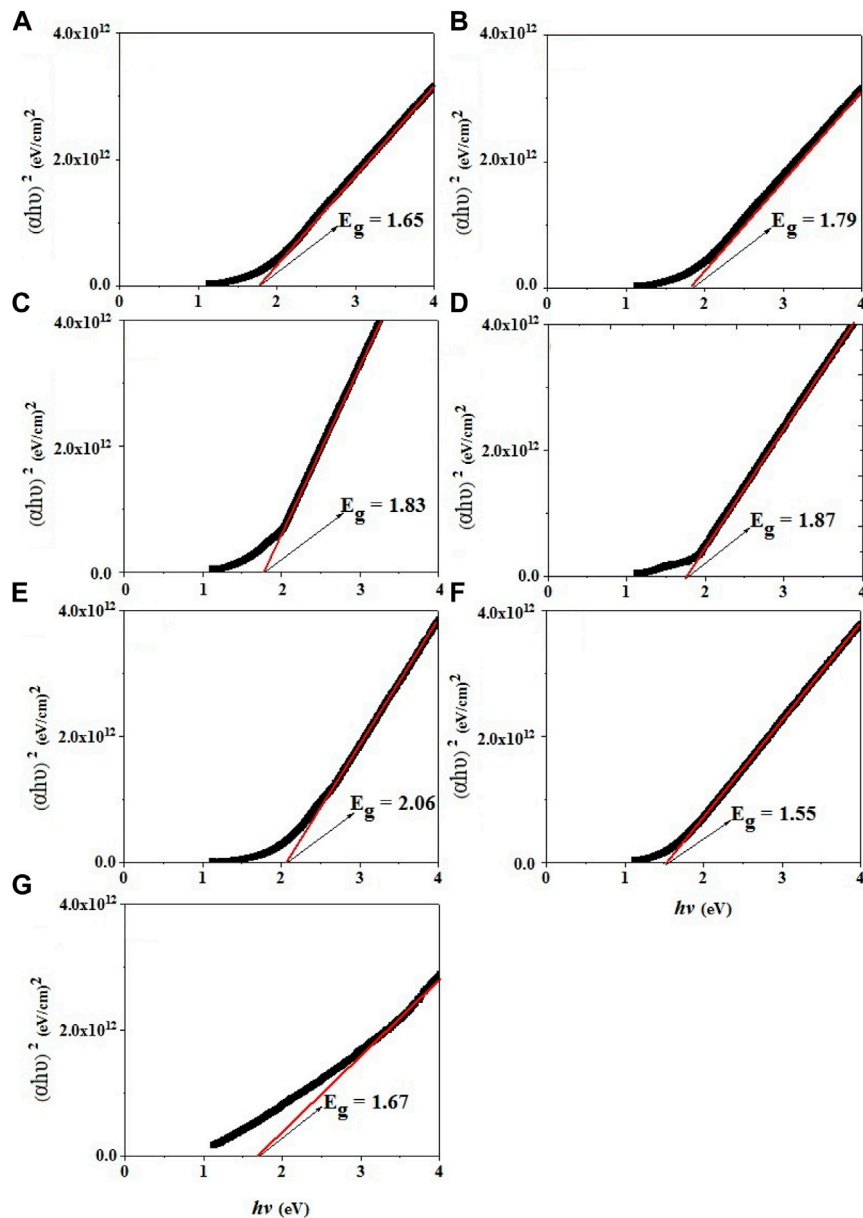
FIGURE 9 | Extrapolation of the linear part of diagram of $(\alpha h\upsilon)^2$ versus $(h\upsilon)$ for $Mg_{0.30-x}Cd_xCu_{0.2}Zn_{0.5}Fe_2O_4$ ferrites **(A)** $x = 0.00$, **(B)** $x = 0.05$, **(C)** $x = 0.10$, **(D)** $x = 0.15$, **(E)** $x = 0.20$, **(F)** $x = 0.25$, **(G)** $x = 0.30$.

of high conductivity grains and grain boundaries that act as insulators. The higher accumulation of electrons at the grain boundary than within the grain results in a more significant bilayer structure and interfacial polarization. At low frequencies, electrons due to transfer and electron exchange between ions can travel more than one atomic distance and pass through the grain and accumulate at the grain boundary. But, the further increase in the frequency causes to change the direction of the electron's motion before reaching the boundaries, resulting in fewer electrons reaching the grain boundary. Hence, the weaker bilayer structure and lower interfacial polarization are created which results in a decrease of dielectric constant (Amini and

Gholizadeh, 2020). As shown in **Figures 10A,B**, the maximum value for the dielectric constant (real and imaginary part) are observed in sample $x = 0.20$ and the lowest value in sample $x = 0.00$. The higher value of the real dielectric constant of sample $x = 0.20$ may be related to its smaller grain size so that at low frequencies, electrons due to easier transfer and electron exchange between Fe^{3+} and M^{2+} ions can pass through the grain and accumulate more at the grain boundary. However, a decrease in the real dielectric constant of sample $x = 0.25$ can also be attributed to the presence of CdO impurity phase.

Figure 10B shows the imaginary part of dielectric constant which means the loss of energy in dielectric materials. As it can be
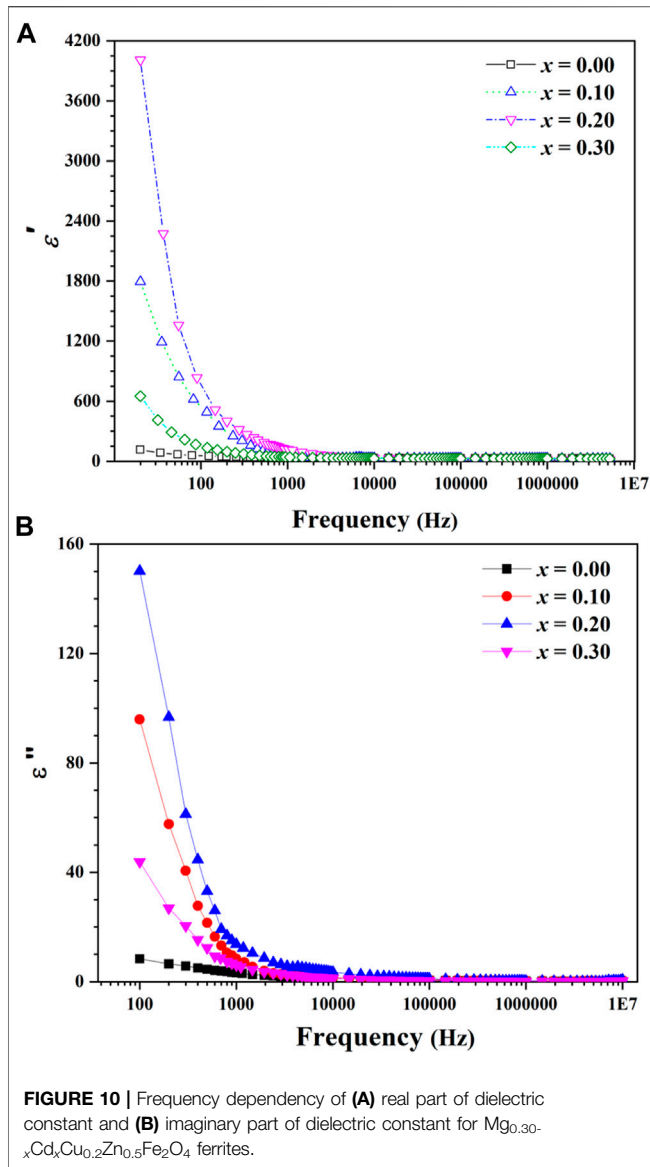
FIGURE 10 | Frequency dependency of **(A)** real part of dielectric constant and **(B)** imaginary part of dielectric constant for $Mg_{0.30-x}Cd_xCu_{0.2}Zn_{0.5}Fe_2O_4$ ferrites.

seen, at low frequencies the loss is very high, and as the frequency increases, the loss decreases steadily. As the frequency increases, the amount of loss reaches a fixed value. High amounts of loss at low frequency can be attributed to the accumulation of electrons in high-resistive grain boundaries. Therefore, much energy is needed to electron transfer between Fe^{3+} and M^{2+} ions. The higher the amount of energy consumed for electron exchange, the greater the energy loss. On the other hand, due to the obvious role of the grain in the electron exchange and the lower resistivity of the grains at higher frequencies, the amount of energy required for electron transfer is reduced and consequently the amount of dielectric loss is reduced (Amini and Gholizadeh, 2020; Beyranvand and Gholizadeh, 2020; Gholizadeh and Beyranvand, 2020). The strong dispersion in the low frequency region and the high value of the measured dielectric constant of sample $x = 0.20$ being large is due to the combined influence of space charge

effects arising from species like Fe^{2+} ions, oxygen vacancies, and grain boundary defects.

Elastic Properties

In the $Mg_{0.30}Cu_{0.2}Zn_{0.5}Fe_2O_4$ ferrites, the Zn^{2+} ions prefer to occupy the tetrahedral sites, while most of the Mg^{2+} and Cu^{2+}ions occupy the octahedral sites. The Fe^{3+} ions are distributed among the tetrahedral and octahedral sites (Shamgani and Gholizadeh, 2019). However, the FTIR results of the samples $Mg_{0.30}Cu_{0.2}Zn_{0.5}Fe_2O_4$ suggest that Cu^{2+} ions prefer to occupy the octahedral sites. Thus the cation distribution for the $Mg_{0.30-x}Cd_xCu_{0.2}Zn_{0.5}Fe_2O_4$ ferrites can be written as $(Zn_{0.5}Fe_{0.5})_A$ $(Cd_xMg_{0.3-x}Cu_{0.2}Fe_{1.5})_B$.

By using molecular weights of cations M_A and M_B on tetrahedral and octahedral sites, the values of force constants K_t and K_o for A- and B-sites, respectively, which suggested by Waldron, were calculated as follow (WALDRON, 1955):

$$K_t\left(\frac{N}{m}\right) = 7.62 \, M_A \, v_t^2 \, 10^{-7} \tag{11}$$

$$K_o\left(\frac{N}{m}\right) = 10.62 \, (M_B/2) \, v_o^2 \, 10^{-7} \tag{12}$$

The stiffness constant C_{11} can be obtained from $K = (K_t + K_o)/2 = a \, C_{11}$ (Gholizadeh, 2017a), where K and a are the average force constant and lattice parameter. In cubic crystals, the other elastic constants of the studied ferrites have been calculated using following equations (WALDRON, 1955; Mohammed et al., 2012; Gholizadeh, 2017a; Dubey and Lahiri, 2021):

$$\text{Velocity of longitudinal wave}: V_L = \sqrt{C_{11}/\rho} \tag{13}$$

$$\text{Velocity of shear wave}: V_S = \sqrt{C_{44}/\rho} = V_L/\sqrt{3} \tag{14}$$

$$\text{Longitudinal Modulus}: L = \rho \, (V_l)^2 \tag{15}$$

$$\text{Rigidity Modulus}: G = \rho \, (V_s)^2 \tag{16}$$

$$\text{Poisson's Ratio}: \sigma = (L - 2G)/(2 \, (L - G)) \tag{17}$$

$$\text{Stiffness constant}: C_{12} = \sigma C_{11}/(1 - \sigma) \tag{18}$$

$$\text{Mean wave velocity}: \frac{3}{V_m^3} = \frac{1}{V_L^3} + \frac{2}{V_S^3} \tag{19}$$

$$\text{Debye temperature}: \theta_D = \frac{hV_m}{k_B}\sqrt[3]{\frac{3\rho qN_A}{4\pi M}} \tag{20}$$

$$\text{Young's modulus}: E = \frac{(C_{11} + 2C_{12})(C_{11} - C_{12})}{(C_{11} + C_{12})} \tag{21}$$

$$\text{Bulk modulus}: B = \frac{(C_{11} + 2C_{12})}{3} \tag{22}$$

where h, k_B, M, q and ρ are the Plank constant, the Boltzmann constant, the molecular weight, the number of atoms in the unit formula and density, respectively. The calculated values for the elastic constants are tabulated in **Table 3**.

It is observed from **Table 3** that the values of the K, C_{11}, C_{44}, C_{12}, L, G, E, and B increase with the increase of Cd^{2+} substitution. It results in increase of the strength of the interatomic interactions between various atoms. This behavior can be attributed to the substitution of heavier Cd^{2+} for lighter Mg^{2+} ions which need higher energy to vibration. The value of $\sigma = 0.2354$ for the

TABLE 3 | Mean force constant (K), elastic stiffness constants (C_{11}, C_{44}, C_{12}), velocity of longitudinal and shear waves (V_L, V_S), mean velocity (V_m) and Debye temperature (Θ_D), longitudinal modulus (L), Poisson's ratio (σ), rigidity modulus (G), Young's modulus (E), and bulk modulus (B) for $Mn_{0.3-x}Ba_xCu_{0.2}Zn_{0.5}Fe_2O_4$ nanoparticles.

Sample	K (N/m)	C_{44} (GPa)	C_{11} (GPa)	C_{12} (GPa)	V_S (m/s)	V_L (m/s)	V_m (m/s)	Θ_D (K)	B (GPa)	G (GPa)	E (GPa)	σ (unitless)	L (GPa)
$x = 0.00$	132.86	52.64	157.93	48.63	3213.2	5462.4	3561.2	512.21	85.04	54.64	135.02	0.23545	157.88
$x = 0.05$	130.00	51.55	154.66	47.62	3149.8	5354.8	3491.1	501.63	83.06	53.51	132.23	0.23545	154.21
$x = 0.10$	131.10	52.01	156.03	48.05	3134.3	5328.3	3473.8	499.43	84.73	53.99	133.41	0.23545	156.04
$x = 0.15$	133.54	52.99	158.98	48.95	3135.0	5329.5	3474.6	499.78	85.35	55.01	135.92	0.23545	158.96
$x = 0.20$	137.50	54.56	163.68	50.40	3153.2	5360.6	3494.8	502.17	88.18	56.63	139.94	0.23545	163.33
$x = 0.25$	139.68	55.41	166.24	51.19	3149.8	5354.7	3491.0	501.88	89.44	57.52	142.13	0.23545	166.04
$x = 0.30$	142.67	56.57	169.73	52.27	3158.2	5369.0	3500.3	502.47	91.19	58.73	145.11	0.23545	169.30

samples lie in the range from -0.9 to 0.5 obtained from the theory of isotropic elasticity (Mohammed et al., 2012; Gholizadeh, 2017a; Dubey and Lahiri, 2021).

Looking at **Table 3**, we can observe that the velocity of shear waves (V_S) is less than longitudinal waves (V_L). This is due to when a wave travels through a material, it makes the particle vibrate. Due to transfer of energy, the vibrating particles collide with other particles, which results in other particles to vibrate. In case of shear waves, vibrates, and hence it requires a larger energy to make the neighboring particle vibrate (Gholizadeh, 2017a). Since, the energy required to vibrate the particle perpendicular to the direction of wave propagation in a material is smaller than parallel vibration; hence the velocity of the shear waves is less than that of longitudinal waves. The values of V_m and θ_D given in **Table 3** for Cd-substituted samples are lower than the pure sample due to the decrease in the wave number of IR bands.

CONCLUSION

In this work, the structural and magnetic properties of $Cd_xMg_{0.30-x}Cu_{0.20}Zn_{0.50}Fe_2O_4$ spinel ferrites prepared by the citrate auto-combustion method were investigated. Rietveld refinement of XRD pattern indicates the formation of a cubic structure with space group $Fd\overline{3}m$ for samples with x up to 0.20, while the impurity phase of CdO is observed in the samples with $x = 0.25$, 0.30. The lattice parameter undergoes a decreasing trend for substitution up to $x = 0.15$ and then increases during the substitution, which can be attributed to the distribution of the cations at the A and B sites. The changes in the particle size obtained from the FESEM images are also consistent with the changes in the a and D_{H-W}. Also, the presence of two υ_1 and υ_2 bands around 450 and 560 cm^{-1} in the FTIR spectra confirms the formation of the spinel structure in the studied ferrites and the results suggested that cadmium is in the B site. An increase of the

Cd^{2+} substitution for Mg^{2+} ions results in a gradual drop in the magnetization of the samples for all substitutions which indicates the presence of non-magnetic Cd^{2+} ions at the B site and the pressure on the Fe^{3+} (5 μ_B) ions at the B site and their transfer to the A site. This reduces the magnetization of the samples according to the Néel relation. Values of the direct energy gap of the samples show a maximum at substitution $x = 0.20$. Changes in the energy gap of the samples can be interpreted in terms of changes in the electronic structure which originated from changes in the metal-oxygen bond length and bond angle. The maximum value for the dielectric constant (real and imaginary part) are observed in sample $x = 0.20$ and the lowest value in sample $x = 0.00$. The higher value of the real dielectric constant of sample $x = 0.20$ may be related to easier transfer and electron exchange between Fe^{3+} and M^{2+} ions due to its smaller grain size.

DATA AVAILABILITY STATEMENT

The original contributions presented in the study are included in the article/Supplementary Material, further inquiries can be directed to the corresponding author.

AUTHOR CONTRIBUTIONS

MB: Formal analysis, resources, methodology, data curation. AZ: Methodology, writing–original draft. AG: Data curation, writing–original draft, writing–review; editing, supervision.

FUNDING

REFERENCES

Abareshi, M., Goharshadi, E. K., Mojtaba Zebarjad, S., Khandan Fadafan, H., and Youssefi, A. (2010). Fabrication, Characterization and Measurement of thermal Conductivity of Fe_3O_4 Nanofluids. *J. Magnetism Magn. Mater.* 322, 3895–3901. doi:10.1016/j.jmmm.2010.08.016

Agrawal, S., Parveen, A., and Azam, A. (2016). Structural, Electrical, and Optomagnetic Tweaking of Zn Doped $CoFe_{2-x}Zn_xO_{4-\delta}$ Nanoparticles. *J. Magnetism Magn. Mater.* 414, 144–152. doi:10.1016/j.jmmm.2016.04.059

Ajmal, M., and Maqsood, A. (2008). Structural, Electrical and Magnetic Properties of $Cu_{1-x}Zn_xFe_2O_4$ Ferrites. *J. Alloys Compd.* 460, 54–59. doi:10.1016/j.jallcom.2007.06.019

Amini, M., and Gholizadeh, A. (2020). Shape Control and Associated Magnetic and Dielectric Properties of $MFe_{12}O_{19}$ (M = Ba, Pb, Sr) Hexaferrites. *J. Phys. Chem. Sol.* 147, 109660. doi:10.1016/j.jpcs.2020.109660

Andrade, A. B., Ferreira, N. S., and Valerio, M. E. G. (2017). Particle Size Effects on Structural and Optical Properties of BaF2 Nanoparticles. *RSC Adv.* 7, 26839–26848. doi:10.1039/c7ra01582h

Bachhav, S. G., Patil, R. S., Ahirrao, P. B., Patil, A. M., and Patil, D. R. (2011). Microstructure and Magnetic Studies of Mg–Ni–Zn–Cu Ferrites. *Mater. Chem. Phys.* 129, 1104–1109. doi:10.1016/j.matchemphys.2011.05.067

Banerjee, M., Verma, N., and Prasad, R. (2007). Structural and Catalytic Properties of $Cu_{1-x}Zn_xFe_2O_4$ Nanoparticles. *J. Mater. Sci.* 42, 1833–1837. doi:10.1007/s10853-006-0821-1

Beyranvand, M., and Gholizadeh, A. (2020). Structural, Magnetic, Elastic, and Dielectric Properties of $Mn_{0.3-x}Cd_xCu_{0.2}Zn_{0.5}Fe_2O_4$ Nanoparticles. *J. Mater. Sci. Mater. Electron.* 31, 5124–5140. doi:10.1007/s10854-020-03073-8

Birajdar, D. S., Devatwal, U. N., Jadhav, K. M., and X-ray, " (2002). IR and Bulk Magnetic Properties of $Cu_{1+x}Mn_xFe_{2-2x}O_4$ Ferrite System. *J. Mater. Sci.* 37, 1443–1448. doi:10.1023/a:1014505620254

Chen, D.-H., and He, X.-R. (2001). Synthesis of Nickel Ferrite Nanoparticles by Sol-Gel Method. *Mater. Res. Bull.* 36, 1369–1377. doi:10.1016/s0025-5408(01)00620-1

Chen, D., Chen, D., Jiao, X., Zhao, Y., and He, M. (2003). Hydrothermal Synthesis and Characterization of Octahedral Nickel Ferrite Particles. *Powder Technol.* 133, 247–250. doi:10.1016/s0032-5910(03)00079-2

Dubey, H. K., and Lahiri, P. (2021). Synthesis, Structural, Dielectric and Magnetic Properties of Cd^{2+} Based Mn Nanosized Ferrites. *Mater. Technol.* 36, 131–144. doi:10.1080/10667857.2020.1734728

El-Kemary, M., Nagy, N., and El-Mehasseb, I. (2013). Nickel Oxide Nanoparticles: Synthesis and Spectral Studies of Interactions with Glucose. *Mater. Sci. Semiconductor Process.* 16, 1747–1752. doi:10.1016/j.mssp.2013.05.018

El-Sayed, A. M. (2002). Effect of Chromium Substitutions on Some Properties of NiZn Ferrites. *Ceramics Int.* 28, 651–655. doi:10.1016/s0272-8842(02)00022-6

Esmaili, L., and Gholizadeh, A. (2020). The Effect of Nd and Zr Co-substitution on Structural, Magnetic and Photocatalytic Properties of $Bi_{1-x}Nd_xFe_{1-x}Zr_xO_3$ Nanoparticles. *Mater. Sci. Semiconductor Process.* 118, 105179. doi:10.1016/j.mssp.2020.105179

Gholizadeh, A. (2017a). A Comparative Study of Physical Properties in Fe_3O_4 Nanoparticles Prepared by Coprecipitation and Citrate Methods. *J. Am. Ceram. Soc.* 100, 3577–3588. doi:10.1111/jace.14896

Gholizadeh, A. (2017b). $La_{1-x}Ca_xCo_{1-y}Mg_yO_3$ Nano-Perovskites as CO Oxidation Catalysts: Structural and Catalytic Properties. *J. Am. Ceram. Soc.* 100, 859–866. doi:10.1111/jace.14602

Gholizadeh, A. (2018). A Comparative Study of the Physical Properties of Cu-Zn Ferrites Annealed under Different Atmospheres and Temperatures: Magnetic Enhancement of $Cu_{0.5}Zn_{0.5}Fe_2O_4$ Nanoparticles by a Reducing Atmosphere. *J. Magnetism Magn. Mater.* 452, 389–397. doi:10.1016/j.jmmm.2017.12.109

Gholizadeh, A., and Beyranvand, M. (2020). Structural, Magnetic, Elastic, and Dielectric Properties of $Mg_{0.3-x}Ba_xCu_{0.2}Zn_{0.5}Fe_2O_4$ Nanoparticles. *Physica B: Condensed Matter* 584, 412079. doi:10.1016/j.physb.2020.412079

Gholizadeh, A., and Jafari, E. (2017). Effects of Sintering Atmosphere and Temperature on Structural and Magnetic Properties of Ni-Cu-Zn Ferrite Nanoparticles: Magnetic Enhancement by a Reducing Atmosphere. *J. Magnetism Magn. Mater.* 422, 328–336. doi:10.1016/j.jmmm.2016.09.029

Gholizadeh, A., and Malekzadeh, A. (2017). Structural and Redox Features of $La_{0.7}Bi_{0.3}Mn_{1-x}Co_xO_3$ Nanoperovskites for Ethane Combustion and CO Oxidation. *Int. J. Appl. Ceram. Technol.* 14, 404–412. doi:10.1111/ijac.12650

Gholizadeh, A., and Tajabor, N. (2010). Influence of N_2- and Ar-Ambient Annealing on the Physical Properties of SnO2:Co Transparent Conducting Films. *Mater. Sci. Semiconductor Process.* 13 (3), 162–166. doi:10.1016/j.mssp.2010.10.004

Gholizadeh, A. (2019). The Effects of A/B-site Substitution on Structural, Redox and Catalytic Properties of Lanthanum Ferrite Nanoparticles. *J. Mater. Res. Technol.* 8, 457–466. doi:10.1016/j.jmrt.2017.12.006

Gholizadeh, A., Yousefi, H., Malekzadeh, A., and Pourarian, F. (2016). Calcium and Strontium Substituted Lanthanum Manganite–Cobaltite $[La_{1-x}(Ca,Sr)_xMn_{0.5}Co_{0.5}O_3]$ Nanocatalysts for Low-Temperature CO Oxidation. *Ceramics Int.* 42, 12055–12063. doi:10.1016/j.ceramint.2016.04.134

Gill, N. K., and Puri, R. K. (1985). Mossbauer Study of $Li_{0.5}Fe_{2.5-x}Cr_xO_4$ Ferrites. *Spectrochimica Acta A: Mol. Spectrosc.* 41, 1005–1008. doi:10.1016/0584-8539(85)80064-7

Gopal Reddy, C., Manorama, S. V., and Rao, V. J. (1999). Semiconducting Gas Sensor for Chlorine Based on Inverse Spinel Nickel Ferrite. *Sensors Actuators B: Chem.* 55, 90–95. doi:10.1016/s0925-4005(99)00112-4

Hakim, M. A., Akhter, S., Paul, D. P., and Hoque, S. M. (2015). Effect of Mg Substituted on Physical and Magnetic Properties of Cu-Mg Ferrites. *Appl. Res. J.* 1, 91–96.

Jauhar, S., Singh, J., Chandra, K., Bansal, S., and Singhal, S. (2011). Structural, Morphological, Magnetic and Optical Properties of Chromium Substituted Strontium Ferrites, $SrCr_xFe_{12-x}O_{19}$ (X = 0.5, 1.0, 1.5, 2.0 and 2.5) Annealed with Potassium Halides. *Powder Technol.* 212, 193–197. doi:10.1016/j.powtec.2011.05.014

Lin, K.-F., Cheng, H.-M., Hsu, H.-C., Lin, L.-J., and Hsieh, W.-F. (2005). Band gap Variation of Size-Controlled ZnO Quantum Dots Synthesized by Sol–Gel Method. *Chem. Phys. Lett.* 409, 208–211. doi:10.1016/j.cplett.2005.05.027

Mahmoudi, S., and Gholizadeh, A. (2018). Effect of Non-magnetic Ions Substitution on the Structure and Magnetic Properties of $Y_{3-x}Sr_xFe_{5-x}Zr_xO_{12}$ Nanoparticles. *J. Magnetism Magn. Mater.* 456, 46–55. doi:10.1016/j.jmmm.2018.02.017

Manikandan, A., Judith Vijaya, J., John Kennedy, L., and Bououdina, M. (2013). Microwave Combustion Synthesis, Structural, Optical and Magnetic Properties of $Zn_{1-x}Sr_xFe_2O_4$ Nanoparticles. *Ceramics Int.* 39, 5909–5917. doi:10.1016/j.ceramint.2013.01.012

Manikandan, A., Judith Vijaya, J., John Kennedy, L., and Bououdina, M. (2013). Structural, Optical and Magnetic Properties of $Zn_{1-x}Cu_xFe_2O_4$ Nanoparticles Prepared by Microwave Combustion Method. *J. Mol. Struct.* 1035, 332–340. doi:10.1016/j.molstruc.2012.11.007

Manikandan, A., Judith Vijaya, J., Sundararajan, M., Meganathan, C., Kennedy, L. J., and Bououdina, M. (2013). Optical and Magnetic Properties of Mg-Doped $ZnFe_2O_4$ Nanoparticles Prepared by Rapid Microwave Combustion Method. *Superlattices and Microstructures* 64, 118–131. doi:10.1016/j.spmi.2013.09.021

Manikandan, A., Kennedy, L. J., Bououdina, M., Vijaya, J. J., and Synthesis, " (2014). Optical and Magnetic Properties O Pure and Co-doped $ZnFe_2O_4$ Nanoparticles by Microwave Combustion Method. *J. Magnetism Magn. Mater.* 349, 249–258. doi:10.1016/j.jmmm.2013.09.013

Mohammed, K. A., Al-Rawas, A. D., Gismelseed, A. M., Sellai, A., Widatallah, H. M., Yousif, A., et al. (2012). Infrared and Structural Studies of $Mg_{1-x}Zn_xFe_2O_4$ Ferrites. *Physica B: Condensed Matter* 407, 795–804. doi:10.1016/j.physb.2011.12.097

Mollamahaleh, Y. B., Hosseini, D., Mazaheri, M., and Sadrnezhaad, S. K. (2011). Surfactant-Free Production of Ni-Based Nanostructures. *Msa* 02, 444–452. doi:10.4236/msa.2011.25059

Navaei Diva, T., Zare, K., Taleshi, F., and Yousefi, M. (2017). Synthesis, Characterization, and Application of Nickel Oxide/CNT Nanocomposites to Remove Pb^{2+} from Aqueous Solution. *J. Nanostruct. Chem.* 7, 273–281. doi:10.1007/s40097-017-0239-0

Noori, F., and Gholizadeh, A. (2019). Structural, Optical, Magnetic Properties and Visible Light Photocatalytic Activity of BiFeO3/graphene Oxide Nanocomposites. *Mater. Res. Express* 6, 1250g1. doi:10.1088/2053-1591/ab6807

Shamgani, N., and Gholizadeh, A. (2019). Structural, Magnetic and Elastic Properties of $Mn_{0.3-x}Mg_xCu_{0.2}Zn_{0.5}Fe_3O_4$ Nanoparticles. *Ceramics Int.* 45, 239–246. doi:10.1016/j.ceramint.2018.09.158

Son, S., Taheri, M., Carpenter, E., Harris, V. G., and McHenry, M. E. (2002). Synthesis of Ferrite and Nickel Ferrite Nanoparticles Using Radio-Frequency thermal Plasma Torch. *J. Appl. Phys.* 91, 7589. doi:10.1063/1.1452705

Thorat, L. M., Patil, J. Y., Nadargi, D. Y., Ghodake, U. R., Kambale, R. C., and Suryavanshi, S. S. (2018). Co^{2+} Substituted Mg–Cu–Zn Ferrite: Evaluation of Structural, Magnetic, and Electromagnetic Properties. *J. Adv. Ceram.* 7, 207–217. doi:10.1007/s40145-018-0272-6

T. Rahal, H., Awad, R., Abdel-Gaber, A. M., and -Said Bakeer, D. E. (2017). Influence of SnO_2 Nanoparticles Incorporation on the Electrochemical Behaviour of a Superconductor in Sodium Sulphate Solutions. *Int. J. Electrochem. Sci.* 12, 10115–10128. doi:10.20964/2017.11.82

Vara Prasad, B. B. V. S. (2015). Effect of Indium Substitution on the Electrical and Magnetic Properties of Ni–Zn Ferrite. *J. Theor. Appl. Phys.* 9, 267–272. doi:10.1007/s40094-015-0185-5

Waldron, R. D. (1955). Infrared Spectra of Ferrites. *Phys. Rev.* 99, 1727–1735. doi:10.1103/physrev.99.1727

William, G. (1944). *Schlecht, "Calculation of Density from X-ray Data, Geological Survey, US Department of Interior"*, 29. Washington: D.C. Am. Mineral., 108–110.

Yue, Z., Zhou, J., Li, L., Wang, X., and Gui, Z. (2001). Effect of Copper on the Electromagnetic Properties of Mg–Zn–Cu Ferrites Prepared by Sol–Gel Auto-Combustion Method. *Mater. Sci. Eng. B* 86, 64–69. doi:10.1016/s0921-5107(01)00660-2

ZeidAbo Zeida, E. F. A., Ibrahem, I. A., Ali, A. M., and Mohamed, W. A. A. (2019). The Effect of CdO Content on the crystal Structure, Surface Morphology, Optical Properties and Photocatalytic Efficiency of P-NiO/n-CdO Nanocomposite. *Results Phys.* 12, 562–570. doi:10.1016/j.rinp.2018.12.009